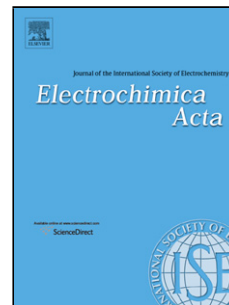


## Accepted Manuscript

Title: Lithium dual uptake anode materials: crystalline Fe<sub>3</sub>O<sub>4</sub> nanoparticles supported over graphite for lithium-ion batteries

Authors: M. Victoria Bracamonte, Emiliano N. Primo, Guillermina L. Luque, Lisandro Venosta, Paula G. Bercoff, Daniel E. Barraco



PII: S0013-4686(17)32092-3  
DOI: <https://doi.org/10.1016/j.electacta.2017.10.034>  
Reference: EA 30420

To appear in: *Electrochimica Acta*

Received date: 29-6-2017  
Revised date: 2-10-2017  
Accepted date: 4-10-2017

Please cite this article as: { <https://doi.org/>

This is a PDF file of an unedited manuscript that has been accepted for publication. As a service to our customers we are providing this early version of the manuscript. The manuscript will undergo copyediting, typesetting, and review of the resulting proof before it is published in its final form. Please note that during the production process errors may be discovered which could affect the content, and all legal disclaimers that apply to the journal pertain.

# Lithium dual uptake anode materials: crystalline $\text{Fe}_3\text{O}_4$ nanoparticles supported over graphite for lithium-ion batteries

M. Victoria Bracamonte<sup>1\*</sup>, Emiliano N. Primo<sup>1+</sup>, Guillermina L. Luque<sup>2</sup>, Lisandro Venosta<sup>1</sup>, Paula G. Bercoff<sup>1</sup>, Daniel E. Barraco<sup>1</sup>

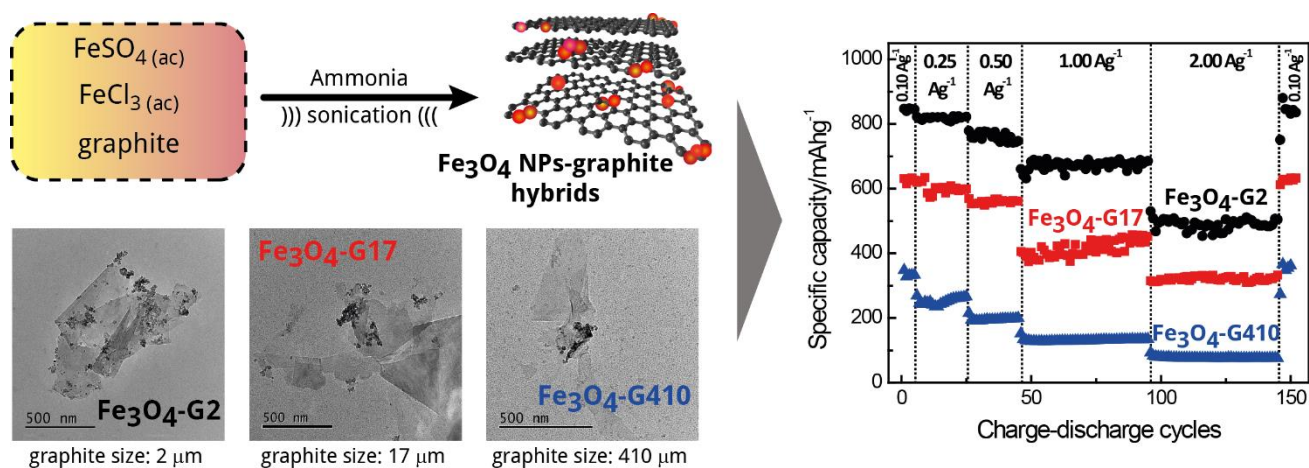
<sup>1</sup>*IFEG, Facultad de Matemática Astronomía y Física, Universidad Nacional de Córdoba, CONICET, Ciudad Universitaria, X5000HUA Córdoba, Argentina.*

<sup>2</sup>*INFIQC, Departamento de Química Teórica y Computacional, Facultad de Ciencias Químicas, Universidad Nacional de Córdoba, CONICET, Ciudad Universitaria, X5000HUA Córdoba, Argentina.*

**Corresponding authors:**

\* [vbracamonte@famaf.unc.edu.ar](mailto:vbracamonte@famaf.unc.edu.ar)

+ [eprimo@famaf.unc.edu.ar](mailto:eprimo@famaf.unc.edu.ar)



Graphical abstract

## HIGHLIGHTS

- Magnetite-graphite hybrids were prepared by a simple and inexpensive synthesis.
- Graphite's flake size defines the edge density and the amount of immobilized  $\text{Fe}_3\text{O}_4$ .
- $\text{Fe}_3\text{O}_4\text{-G}$  films' morphology controls the electrochemical properties of the anodes.
- The deposition of  $\text{Fe}_3\text{O}_4$  plays an important role in the electrochemical performance.
- The anode with the smallest graphite particle size delivers a capacity of 845  $\text{mAhg}^{-1}$ .

## Abstract

Graphite, the usual anode material for current technology of lithium ion batteries (LIB), has great advantages and its processing is widely known and industrially feasible. For improving the anode's capacity, recent research has focused in using nano-carbons as an overcoming strategy rather than including cheap, conversion-type oxide metals. Here, we present the application of in-situ synthesized hybrid LIB active anode materials composed of magnetite nanoparticles ( $\text{Fe}_3\text{O}_4$  NPs) and graphite of different sizes. The results show that the graphite's flake size plays an important role in the  $\text{Fe}_3\text{O}_4$  NPs

deposition and loading, and therefore in the morphology of the resulting laminate film. The electrochemical performance (evaluated by cyclic voltammetry, galvanostatic charge/discharge cycles and impedance spectroscopy) is determined not only by the edge density of graphite flakes and  $\text{Fe}_3\text{O}_4$  loading but also by the porosity of the anode films. The hybrid material electrode with smallest graphite particle size shows the highest reversible capacity of  $845 \text{ mA h g}^{-1}$ , good rate capability and great cycling performance. This remarkable improvement in graphite's capacity is reached by only adding 16 wt% of magnetite to the carbon material.

## Keywords

$\text{Fe}_3\text{O}_4$  nanoparticles, graphite, dual anodes, lithium-ion batteries, hybrid materials

## 1. INTRODUCTION

Li-ion batteries (LIB) have an unmatched combination of high energy and power density, making them the first choice in technology for portable electronics, power tools, energy harvesting and hybrid/full electric vehicles [1,2]. To meet these requirements, current LIB technology must increase its energy density, which can be straightforwardly accomplished by developing high-voltage cathodes or high-capacity anodes [3]. Commercially available LIB anodes use graphite as active material, whose  $372 \text{ mA h g}^{-1}$  capacity needs to be increased for such applications. In this sense, nature-abundant transition metal oxides have been investigated as promising high-capacity anodes [1,4–6]. Among them, magnetite ( $\text{Fe}_3\text{O}_4$ ) has a special interest for being low cost and environmentally friendly. This metal oxide undergoes a conversion reaction with  $\text{Li}^+$  ions which results in a theoretical capacity of  $924 \text{ mA h g}^{-1}$ , almost 3 times larger than the industry-standard graphite [5,7,8].

During lithiation,  $\text{Fe}_3\text{O}_4$  undergoes a complex process involving multiple phase transitions that are strongly dependent on the electrochemical environment and  $\text{Li}^+$  diffusion through the channels of

the dense crystalline structure of magnetite [9,10]. Besides, the almost electric insulant nature of bulk  $\text{Fe}_3\text{O}_4$  makes its use as anode highly disadvantageous due to large polarization and sloping voltage profiles. In fact, structural change and volume expansion are associated with the  $\text{Fe}_3\text{O}_4$  conversion mechanism, eventually leading to pulverization and loss of contact between active material particles [5,8,11]. To circumvent these issues, the use of  $\text{Fe}_3\text{O}_4$  nanoparticles [8,12] and nanometer scale  $\text{Fe}_3\text{O}_4$ -based structures in combination with conductive material substrates (mainly carbon-based) are almost mandatory to attain exceptional high capacity and high cyclability properties of magnetite [5,8,11,13–16]. In this way,  $\text{Fe}_3\text{O}_4$  nanocrystalline structures such as hollow spheres [17,18], nanowires [19,20], pomegranate/hierarchical structures [21–23] and different polyhedra [12,24,25] have been used for the development of LIB anodes. These varied structures were also combined with nano-allotropes derived from carbon, including carbon nanotubes [26–28], graphene-derived materials [29–33], nano-onions [34] and nanoshells [13,35,36].

Although the benefits of using nano-carbons/magnetite hybrids are truly remarkable and widespread, the excellent properties of current graphite battery grade technology as anode for LIB should not be underestimated. Graphite's high volumetric capacity, low average voltage and voltage hysteresis, good rate capability, good thermal stability when low surface area is maintained, low volume expansion during lithiation, and excellent densification properties in electrode coatings makes it almost a “miraculous material”, quite difficult to be outmatched from the economic and industrial points of view [37–39]. In this way, the challenge for immediate commercial application of novel strategies is how to improve graphite's lithium-capacity properties without losing considerably its other advantages.

In this work, we present the in-situ modification of graphite flakes of different sizes with  $\text{Fe}_3\text{O}_4$  nanoparticles (NPs) as hybrid active materials for LIB anodes. Amongst the various strategies of  $\text{Fe}_3\text{O}_4$  NPs syntheses [40,41], our methodology is simple, effortless and quite inexpensive. The synthesized hybrids (reported previously by our group [42]) were further characterized in terms of the carbon

support. The electrochemical performance, cyclability and charge-discharge profiles were compared taking advantage of the lithiation capacity that both Fe<sub>3</sub>O<sub>4</sub> NPs and graphite have. Electrochemical impedance spectroscopy in combination with spectroscopic and thermogravimetric analyses revealed a dependency between Fe<sub>3</sub>O<sub>4</sub> loading, capacity and density of edge in the graphite samples. The hybrid with the smallest graphite particle size is the one that showed the highest specific capacity and the best capacity retention, even at high current densities, by only adding 16 wt% of magnetite.

## **2. EXPERIMENTAL**

### **2.1. Materials and chemicals**

Graphite powder (particle size ~17 μm) and graphite flakes (particle size ~410 μm) were purchased from Sigma. Graphite Micrograf was from Nacional de Grafito (size ~2 μm). Iron (II) sulphate heptahydrated was from Sigma and Iron (III) chloride hexahydrated was from Anedra. Sodium alginate polymer was from Sigma and TIMCAL carbon superP was from MTI Technologies. Other reagents were battery grade and were used without further purification.

### **2.2. Synthesis of Fe<sub>3</sub>O<sub>4</sub> nanoparticles on graphite substrates**

The ultrasound-assisted Fe<sub>3</sub>O<sub>4</sub> NPs synthesis on different carbon matrices was performed according our previous work [42]. Briefly, 1.0 mL of 0.20 M FeSO<sub>4</sub> solution and 4.0 mL of 0.10 M FeCl<sub>3</sub> solution were mixed and then 0.30 g of the graphitic material was added. The mixed Fe<sup>2+</sup>/Fe<sup>3+</sup> solution was sonicated for 30 min in an ultrasonic bath. Afterwards, 18.0 mL of 0.70 M ammonia were added drop-wise to the mixture and sonicated for another 30 min. The generated Fe<sub>3</sub>O<sub>4</sub>-graphite hybrids were collected by magnetic separation, washed, filtered and dried at 80 °C in vacuum for 18 h. The obtained samples were labeled according to the graphite particle size: Fe<sub>3</sub>O<sub>4</sub>-G2 (graphite Micrograf), Fe<sub>3</sub>O<sub>4</sub>-G17 (graphite powder) and Fe<sub>3</sub>O<sub>4</sub>-G410 (graphite flakes). Figure S1 (in the

Supporting Information) shows SEM images and the corresponding flake size histograms obtained for the different graphites, after processing several images.

### 2.3. Electrodes preparation and electrochemical characterization

The slurry was composed of active Fe<sub>3</sub>O<sub>4</sub>-graphite hybrids (70 wt%), TIMCAL carbon superP (15 wt%) and sodium alginate binder (15 wt%); the solvent was 0.10 M citric acid buffer solution pH 3.00. All these components were physically mixed in a ball mill before being doctor-blade casted onto a copper foil. The active material mass loading ranged from 0.62 to 0.80 mg cm<sup>-2</sup> and the electrode laminates had an average thickness of 13, 17 and 32 μm for Fe<sub>3</sub>O<sub>4</sub>-G2, Fe<sub>3</sub>O<sub>4</sub>-G17 and Fe<sub>3</sub>O<sub>4</sub>-G410, respectively. For comparative purposes, a slurry was made with Fe<sub>3</sub>O<sub>4</sub> NPs alone, without any supporting graphite, in the same weight proportion than the other samples, by completing with TIMCAL carbon superP.

The electrochemical performance of the electrodes was characterized in a CR 2032-type coin cell configuration using Celgard 2325 as the separator and a lithium foil as the counter electrode. The electrolyte consisted of a 50 % v/v mix of ethylene carbonate and ethyl methyl carbonate, with 1.00 M LiPF<sub>6</sub>. Galvanostatic charge-discharge profiles, cyclic voltammetry (CV) and impedance spectroscopy (EIS) experiments were performed with an Arbin battery cycler (Arbin Instruments, USA) and an Autolab PGSTAT320N Potentiostat/Galvanostat (Metrohm, The Netherlands), respectively. EIS data were fitted with ZView software and normalized by the electrode's geometric area and the active material mass. Specific capacities (expressed in mA h g<sup>-1</sup>) were calculated in terms of the total mass of graphite-Fe<sub>3</sub>O<sub>4</sub> active material.

### 2.4. Physico-chemical characterization

X-ray diffraction (XRD) patterns were obtained in a Philips PW1800/10 diffractometer operated at 40 kV and 30 mA with a Cu-Kα radiation source. Scanning electron microscopy (SEM) images were obtained with a field emission scanning electron microscope FE-SEM, Sigma Zeiss

(LAMARX facilities) working at 5 kV. Transmission electron microscopy images (TEM) were obtained using a JEOL JEM 2100 transmission electron microscope operating at an accelerating voltage of 200 kV. Several drops of the ethanol solutions of the samples were placed on a 100 mesh copper grid coated with a Formvar film. The size distribution of the nanoparticles was obtained by averaging the sizes of several particles directly from the TEM images using the Image-J software. Thermogravimetric analyses (TGA) of approximately 5 mg of each compound were recorded on a TGA Q600 (TA Instruments) under air atmosphere, by equilibrating at 100°C, and following a heating ramp rate of 10°C min<sup>-1</sup> up to 800°C.

### 3. RESULTS AND DISCUSSION

#### 3.1. Structure and morphology characterization

*[Figure 1]*

TEM images for Fe<sub>3</sub>O<sub>4</sub>-G2, Fe<sub>3</sub>O<sub>4</sub>-G17 and Fe<sub>3</sub>O<sub>4</sub>-G410 are shown in panels **A**, **B** and **C** of **Figure 1**, respectively. The photographs show the different graphite flakes covered with (14 ± 2) nm diameter Fe<sub>3</sub>O<sub>4</sub> NPs (the particles' image and the corresponding size histogram are depicted in Figure S2). A higher nanoparticle coverage is observed in the samples with smaller graphite flakes size and a preferential immobilization at the edges of the structure. In our previous work [42], we determined through Raman spectroscopy and magnetic measurements that the amount of magnetite deposited on each substrate depends on the defects density, being the carbon substrates with smaller particle sizes more effective for Fe<sub>3</sub>O<sub>4</sub> NPs immobilization. The possible defects include edges, topological defects, vacancies and substitutional impurities which are all capable of having oxygen-rich groups that could act as nucleation spots for the Fe<sub>3</sub>O<sub>4</sub> NPs deposition [14].

The effect in the laminates morphology at the Cu foil of the different hybrid materials are shown in the SEM images of **Figure 1** (panel **D**, **E** and **F**). In all of them, the thin irregularly shaped graphite flakes surrounded by round-shaped carbon superP particles can be observed. The smaller the graphite flake size, the more randomized its distribution, and the higher the amount of edges exposed. Tentatively, this would imply a higher cross sectional area for electrochemical processes per  $1 \text{ cm}^2$  of geometric area of the electrode, as Li ions intercalate through the graphite side rather than the basal planes. Also, the porosity (taken as the relative number of voids and irregularities) increases according to  $\text{Fe}_3\text{O}_4\text{-G2} < \text{Fe}_3\text{O}_4\text{-G17} < \text{Fe}_3\text{O}_4\text{-G410}$ : for the latter a highly compact film can be seen with the appearance of cracks (**Figure 1 F**).

*[Figure 2]*

The XRD patterns of **Figure 2** for the  $\text{Fe}_3\text{O}_4\text{-G2}$  (**a**),  $\text{Fe}_3\text{O}_4\text{-G17}$  (**b**) and  $\text{Fe}_3\text{O}_4\text{-G410}$  (**c**) slurries further confirm the presence of graphite and magnetite at the anodes. The reflection peaks at  $2\theta = 30.1^\circ$  and  $35.6^\circ$  correspond to the planes (2 2 0) and (3 1 1) of  $\text{Fe}_3\text{O}_4$  cubic structure. The reflection peaks at  $2\theta = 26.5^\circ$  and  $54.6^\circ$  correspond to the planes (0 0 2) and (0 0 4) of graphite's hexagonal crystallographic system. The  $2\theta$  region between  $42^\circ$  and  $47^\circ$  is associated with the (1 0 0) and (1 0 1) graphite's reflections, and the (4 0 0) planes of magnetite. In this case, due to the peaks overlap, is not possible to unambiguously index them (Figure S3 in the Supporting Information depicts the XRD patterns of pure graphite and magnetite). The crystallite sizes of magnetite in the samples were estimated through the Scherrer formula, giving a value of 11 nm for every sample, in good agreement with the diameter determined by TEM. By comparing the peaks corresponding to magnetite in the slurries' XRD patterns with the as-synthesized  $\text{Fe}_3\text{O}_4$  diffractogram (Figure S3 d), it can be concluded that the high-energy ball milling procedure used to prepare electrodes does not affect the crystalline structure of magnetite as active material or generates any other Fe-related crystalline phase (within the detection limit of this technique).

[Figure 3]

[Table 1]

**Figure 3** presents TGA curves, performed in air, for the three graphites (in dashed lines) and the corresponding Fe<sub>3</sub>O<sub>4</sub> hybrid materials (in full lines). In the pure graphite samples, the observed weight loss is due to the oxidation of carbon. Upon decreasing the particle size of the graphitic material, the edge density increases, therefore decreasing the onset temperature (T<sub>O</sub>), as seen in the first column of **Table 1**. In the thermograms of the Fe<sub>3</sub>O<sub>4</sub>-G hybrids, after the weight loss of graphite, the profiles stabilize as magnetite does not experience any thermal-induced modification in the analyzed temperature range (Figure S4, in the Supporting Information). This allowed to obtain the Fe<sub>3</sub>O<sub>4</sub>-loadings for each sample, which are disclosed in the last column of **Table 1**. As graphite G2 is the one with the highest defect density, it has the largest amount of immobilized magnetite. It is interesting to note that the presence of the Fe<sub>3</sub>O<sub>4</sub> NPs significantly lowers the graphite's T<sub>O</sub> (**Table 1**). The decreased combustion temperature is likely due to the presence of the catalytic Fe<sub>3</sub>O<sub>4</sub> NPs, and it is an indication of the intimate interfacing between them and the graphite edges. This effect has also been observed in other hybrid materials modified with nanoparticles, which act as “hot spots” favoring carbon calcination [43,44].

### 3.2. Electrochemical characterization and anodes performance

[Figure 4]

The anodes prepared with the Fe<sub>3</sub>O<sub>4</sub>-G hybrids were assembled into coin-type cells to evaluate their electrochemical Li-storage performance. **Figure 4 A, B and C** illustrate the first and fifth voltammograms for Fe<sub>3</sub>O<sub>4</sub>-G2, Fe<sub>3</sub>O<sub>4</sub>-G17 and Fe<sub>3</sub>O<sub>4</sub>-G410; respectively. In all the samples and during the first cathodic scan, a broad peak starts to evolve at ~ 0.800 V. The first process that contributes to this peak is the formation of the solid electrolyte interface (SEI) [45]. The second one, is associated to the conversion reaction of magnetite, which consists of an initial irreversible step where

lithium ions insert into the  $\text{Fe}_3\text{O}_4$  structure (equation (1)) and then it further proceeds to the formation of metallic Fe NPs and  $\text{Li}_2\text{O}$  (equation (2)) [10].



After magnetite fully reacted with  $\text{Li}^+$ , another steep peak appears in all the voltammograms below 0.200 V, due to the intercalation reaction (equation (3)) of graphite [46,47]. Upon reversing the scan, the sharp peak of graphite reversible delithiation can be observed and, afterwards, a broad peak between 0.900-2.400 V appears, corresponding to the redox conversion of lithium oxide and metallic iron to the  $\text{Li}_x\text{Fe}_3\text{O}_4$  phase. The initial  $\text{Fe}_3\text{O}_4$  is never formed again [8,10,11]. This can be evidenced in the subsequent cycles, where the cathodic conversion process appears at higher voltages for all the materials (marked with the red lines) and remains unaltered throughout the cycling (the CV profile of a  $\text{Fe}_3\text{O}_4$  anode is displayed in Figure S5 A). By comparing the CV profiles of panels **A**, **B** and **C** it is clear that as the size of graphite particles is reduced, the specific current of lithiation/delithiation processes increases. This is due to an increase in the edge density of graphite (and therefore the amount of intercalable regions that uptake Li ions) and in the density of  $\text{Fe}_3\text{O}_4$  active nanoparticles.

*[Figure 5]*

*[Table 2]*

**Figure 5** shows the representative galvanostatic lithiation profiles of  $\text{Fe}_3\text{O}_4$ -G2 (**A**),  $\text{Fe}_3\text{O}_4$ -G17 (**B**) and  $\text{Fe}_3\text{O}_4$ -G410 (**C**) at a current density of  $0.10 \text{ A g}^{-1}$  between 3.000 and 0.010 V. In consonance with CV results, the voltage interval between 1.500 and 0.300 V (red-shaded regions in the voltage and  $\partial Q/\partial V$  profiles) corresponds to the reversible  $\text{Fe}_3\text{O}_4$  lithiation reaction. In the grey-shaded regions of the hybrid anodes profiles (below 0.250 V), the intercalation of Li ions into graphite takes place.

For comparison purposes, Figure S5 B and C exhibit the typical galvanostatic charge-discharge profiles for Fe<sub>3</sub>O<sub>4</sub> and the three different graphite samples, respectively.

In general, the hybrid materials exhibit good coulombic efficiencies, and Fe<sub>3</sub>O<sub>4</sub>-G2 is the one that holds the greatest specific capacity (**Table 2**). The last column of the table displays the contribution of the Fe<sub>3</sub>O<sub>4</sub> conversion reaction (i.e., the red-shaded capacity regions of **Figure 5**) to the total capacity of each anode. The observed trend in the percentages is associated to the ratio between graphite's edges and Fe<sub>3</sub>O<sub>4</sub> loading. As schemed in Figure S6, there is a decrease in graphite size while the amount of magnetite remains almost unaltered from Fe<sub>3</sub>O<sub>4</sub>-G410 to Fe<sub>3</sub>O<sub>4</sub>-G17, reducing the contribution of Fe<sub>3</sub>O<sub>4</sub> to the total capacity (from 43 to 34%) and increasing the contribution of graphite to the total capacity, due to the larger amount of edges available for lithiation. In the case of Fe<sub>3</sub>O<sub>4</sub>-G2, the graphite's edge density is very similar to that of Fe<sub>3</sub>O<sub>4</sub>-G17 but magnetite loading rises, therefore increasing its contribution to the total capacity.

It is worth noting that, regardless the hybrid material, the contribution to the total capacity of Fe<sub>3</sub>O<sub>4</sub> is higher than its mass loading in the hybrids (between 11 and 16%). Specific capacity for Fe<sub>3</sub>O<sub>4</sub> is 2.5 times larger than graphite, as magnetite can store up to 8 Li per unit formula while carbon only 1/6. This is where the main advantage of adding magnetite to graphite resides: by slightly increasing the mass of the anode we gain a great boost in the specific capacity. Another intriguing aspect of these hybrids is the additional reversible capacity shown beyond the theoretical 945 mA h g<sup>-1</sup>. If we take the capacity solely from Fe<sub>3</sub>O<sub>4</sub> conversion reaction and normalize it by magnetite's mass loading, Fe<sub>3</sub>O<sub>4</sub> specific capacity in G2, G17 and G410 hybrids is, respectively, 1415, 1256 and 1099 mA h g<sup>-1</sup>. These increased capacities are extensively informed in bibliography, were most of the reported Fe<sub>3</sub>O<sub>4</sub>-based anodes have similar values [8,15,16]. In a conversion-type anode study [48] it was demonstrated that the formation of LiOH at the active particles' surface can provide additional charge storage from the reaction  $\text{LiOH} + 2 \text{Li} \leftrightarrow \text{Li}_2\text{O} + \text{LiH}$ . The origin of this LiOH comes from either the electrolyte decomposition (the Fe NPs formed during anode lithiation can catalyse such process) or from the

presence of a native OH layer at Fe<sub>3</sub>O<sub>4</sub> NPs. The presence of OH groups can be evidenced through Raman and FTIR spectra of the hybrids, as shown in Figure S7. Besides E<sub>g</sub>, T<sub>2g</sub>(2) and A<sub>2g</sub> first-order bands of magnetite in the Raman spectra, the FTIR reveals two bands around 880 and 790 cm<sup>-1</sup>. These can be assigned to Fe-O-H bending vibrations of surface FeOOH groups [49]. Therefore, the presence of surface hydroxyl groups due to the alkaline conditions of the hybrids syntheses could explain the formation of LiOH and the corresponding increase in the specific capacity.

*[Figure 6]*

The Fe<sub>3</sub>O<sub>4</sub>-G hybrid anodes were further tested at different current densities and the resulting specific capacities and coulombic efficiencies at each rate are depicted in **Figure 6**. The Fe<sub>3</sub>O<sub>4</sub>-G2 hybrid exhibits the best rate performance in terms of specific capacity, even at high current densities such as 2.00 A g<sup>-1</sup>, where the capacity is 485 mA h g<sup>-1</sup> compared to 310 mA h g<sup>-1</sup> and 80 mA h g<sup>-1</sup> for the Fe<sub>3</sub>O<sub>4</sub>-G17 and Fe<sub>3</sub>O<sub>4</sub>-G410 anodes, respectively. Despite the material under analysis, all of them display a good coulombic efficiency and excellent reversibility, as after heavy testing at various rates for 150 cycles the capacity is restored to the initial values at a current density of 0.10 A g<sup>-1</sup>. The charge-discharge profiles corresponding to the different current densities are presented in Figure S8.

In addition, the electrochemical performance of the in-situ synthesized hybrids were compared to homologous anodes prepared by physical mixture of G2, G17 and G410 with Fe<sub>3</sub>O<sub>4</sub> NPs, maintaining the same weight proportion and preparation methodology as the hybrids (shown in Figure S9 in the Supporting Information). In all the cases, the anodes based on the chemically prepared hybrids present a better performance, less capacity fade and greater capacities than the anodes prepared by physical mixture, indicating that the close contact and selective deposition of the magnetite NPs near the edges of graphite flakes through the in-situ synthesis is highly beneficial and necessary for attaining the outstanding cyclability.

*[Figure 7]*

**Figure 7** depicts the EIS spectra of the anodes at 3.000 V (delithiated, panel **A**) and at 0.010 V (lithiated, panel **B**). EIS spectra of delithiated anodes were modelled with the equivalent circuit shown in **Scheme 1**. It consists of an ohmic resistance ( $R_0$ ) corresponding to the high-frequency zero crossing in the Nyquist plots, a first parallel circuit ( $R_{SEI} \parallel Q_{SEI}$ ) related to the influence of the SEI on the  $Li^+$  migration in the high frequency region, a second parallel circuit ( $R_{ct} \parallel Q_{ct}$ ) ascribed to the charge transfer reaction due to  $Li^+$  intercalation/conversion at mid-frequencies, and a Warburg diffusion element ( $W$ ) at low frequencies [47]. The EIS spectra of panel **B** were fitted with the circuit presented in **Scheme 2**: in this case, instead of  $W$  element a low frequency semicircle appears, corresponding to the parallel circuit ( $R_{pore} \parallel Q_{pore}$ ). This process arises due to the presence of porous sublayers through the composite electrode, as a consequence of a non-oriented distribution of graphite particles and the formation of pores [50].

*[Scheme 1]*

*[Scheme 2]*

Both  $R_{ct}$  and  $R_{SEI}$  (depicted in panel **A** and **B** of **Figure 8**, respectively) increase with the graphite flake size of the hybrids: the amount of  $Fe_3O_4$  loading and cross sectional area for electrochemical processes increase for smaller sizes, which favours charge transfer and generates a more stable and conductive SEI. These conclusions are in agreement with the CV and galvanostatic charge/discharge previously shown. It is noteworthy that the resistances rise from the delithiated to the fully lithiated state, by comparing black and red bars in panels **A** and **B**. The explanation for this behavior in the electrodes' impedance at low potentials is related to an increase in the  $Li^+$  concentration in the  $Fe_3O_4$ -G side, which slows down the rate of  $Li^+$  migration through the surface films because of a decrease in the potential drop across the graphite/film/solution interface [47].

*[Figure 8]*

The porous structure of the anode films on the Cu foil generates the characteristic low frequency semicircle that gives further insights for understanding the better performance of the smaller flake size hybrid. **Figure 8 C** displays  $R_{\text{pore}}$  and  $Q_{\text{pore}}$  for each electrode, showing that upon reducing the  $\text{Fe}_3\text{O}_4$ -G particle size, the resistance diminishes and the capacitance grows. SEM images of **Figure 1 D, E and F** (and thickness measurements) revealed that the porosity was higher for  $\text{Fe}_3\text{O}_4$ -G2 anodes while  $\text{Fe}_3\text{O}_4$ -G410 laminate was very compact. Therefore, the films' morphology also controls the electrochemical properties of the anodes, since for the most porous  $\text{Fe}_3\text{O}_4$ -G2 electrode,  $R_{\text{pore}}$  is lower and  $Q_{\text{pore}}$  is the highest as a consequence of its greater effective electroactive area for  $\text{Li}^+$  diffusion and charge transfer.

#### 4. CONCLUSIONS

$\text{Fe}_3\text{O}_4$ -G hybrid materials were successfully synthesized using different graphite particle sizes. The as-synthesized hybrids were used as anode materials for LIBs, exhibiting an excellent cycling capability and rate performance. It is found that the different graphite flakes sizes determine not only the amount of immobilized magnetite, but also the film morphology. These aspects modify the electrochemical performance of the  $\text{Fe}_3\text{O}_4$ -G anodes, obtaining the best response with the smallest graphite size and a percentage of only 16% of the immobilized magnetite. This behavior is explained considering that the amount of  $\text{Fe}_3\text{O}_4$  loading and cross-sectional area for electrochemical processes increase when reducing the graphite's size, favoring the charge transfer and generating a more stable and conductive SEI, as a result of the great synergy between these two materials. The chemically obtained hybrids present a better electrochemical performance in comparison with the counterparts obtained by physical mixing, showing the great connection between magnetite nanoparticles and graphite. In terms of specific capacity, the best response is obtained using  $\text{Fe}_3\text{O}_4$ -G2 as anode, which had 845 and 485  $\text{mA h g}^{-1}$  at current densities of 0.10 and 2.00  $\text{A g}^{-1}$ , respectively. All these

characteristics make this material a great promise for improving electrochemical performance of graphite-based anodes in lithium ion batteries.

## Acknowledgements

The authors acknowledge partial financial support for this research from Y-TEC, Secyt-UNC, ANPCyT and CONICET. The authors thank Dr. Hernandez and Dr. Nome for assisting with TEM measurements.

## References

- [1] N. Nitta, F. Wu, J.T. Lee, G. Yushin, Li-ion battery materials: Present and future, *Mater. Today*. 18 (2015) 252–264. doi:10.1016/j.mattod.2014.10.040.
- [2] A. Opitz, P. Badami, L. Shen, K. Vignarooban, A.M. Kannan, Can Li-Ion batteries be the panacea for automotive applications?, *Renew. Sustain. Energy Rev.* 68, Part 1 (2017) 685–692. doi:https://doi.org/10.1016/j.rser.2016.10.019.
- [3] R. Amirante, E. Cassone, E. Distaso, P. Tamburrano, Overview on recent developments in energy storage: Mechanical, electrochemical and hydrogen technologies, *Energy Convers. Manag.* 132 (2017) 372–387. doi:https://doi.org/10.1016/j.enconman.2016.11.046.
- [4] P. Poizot, S. Laruelle, S. Grugeon, L. Dupont, J.-M. Tarascon, Nano-sized transition-metal oxides as negative-electrode materials for lithium-ion batteries, *Nature*. 407 (2000) 496–499. http://dx.doi.org/10.1038/35035045.
- [5] S.-H. Yu, S.H. Lee, D.J. Lee, Y.-E. Sung, T. Hyeon, Conversion Reaction-Based Oxide Nanomaterials for Lithium Ion Battery Anodes, *Small*. 12 (2016) 2146–2172. doi:10.1002/sml.201502299.
- [6] D. Bresser, S. Passerini, B. Scrosati, Leveraging valuable synergies by combining alloying and conversion for lithium-ion anodes, *Energy Environ. Sci.* 9 (2016) 3348–3367. doi:10.1039/C6EE02346K.
- [7] A. Eftekhari, Lithium-Ion Batteries with High Rate Capabilities, *ACS Sustain. Chem. Eng.* 5 (2017) 2799–2816. doi:10.1021/acssuschemeng.7b00046.
- [8] A.M. Bruck, C.A. Cama, C.N. Gannett, A.C. Marschilok, E.S. Takeuchi, K.J. Takeuchi, Nanocrystalline iron oxide based electroactive materials in lithium ion batteries: the critical role of crystallite size, morphology, and electrode heterostructure on battery relevant electrochemistry, *Inorg. Chem. Front.* 3 (2016) 26–40. doi:10.1039/C5QI00247H.
- [9] A. Abraham, L.M. Housel, C.N. Lininger, D.C. Bock, J. Jou, F. Wang, A.C. West, A.C. Marschilok, K.J. Takeuchi, E.S. Takeuchi, Investigating the Complex Chemistry of Functional Energy Storage Systems: The Need for an Integrative, Multiscale (Molecular to Mesoscale) Perspective, *ACS Cent. Sci.* 2 (2016) 380–387. doi:10.1021/acscentsci.6b00100.
- [10] K. He, S. Zhang, J. Li, X. Yu, Q. Meng, Y. Zhu, E. Hu, K. Sun, H. Yun, X.-Q. Yang, Y. Zhu, H. Gan, Y. Mo, E.A. Stach, C.B. Murray, D. Su, Visualizing non-equilibrium lithiation of spinel oxide via in situ transmission electron microscopy, *Nat. Commun.* 7 (2016) 11441. http://dx.doi.org/10.1038/ncomms11441.

- [11] Q. Su, S. Wang, Y. Xiao, L. Yao, G. Du, H. Ye, Y. Fang, Lithiation Behavior of Individual Carbon-Coated Fe<sub>3</sub>O<sub>4</sub> Nanowire Observed by in Situ TEM, *J. Phys. Chem. C*. 121 (2017) 3295–3303. doi:10.1021/acs.jpcc.6b12973.
- [12] Q. Wang, D. Chen, J. Chen, C. Lai, L. Li, C. Wang, Facile synthesis and electrochemical properties of Fe<sub>3</sub>O<sub>4</sub> hexahedra for Li-ion battery anode, *Mater. Lett.* 141 (2015) 319–322. doi:https://doi.org/10.1016/j.matlet.2014.11.103.
- [13] X. Qin, H. Zhang, J. Wu, X. Chu, Y.-B. He, C. Han, C. Miao, S. Wang, B. Li, F. Kang, Fe<sub>3</sub>O<sub>4</sub> nanoparticles encapsulated in electrospun porous carbon fibers with a compact shell as high-performance anode for lithium ion batteries, *Carbon N. Y.* 87 (2015) 347–356. doi:https://doi.org/10.1016/j.carbon.2015.02.044.
- [14] T.N. Narayanan, Z. Liu, P.R. Lakshmy, W. Gao, Y. Nagaoka, D. Sakthi Kumar, J. Lou, R. Vajtai, P.M. Ajayan, Synthesis of reduced graphene oxide–Fe<sub>3</sub>O<sub>4</sub> multifunctional freestanding membranes and their temperature dependent electronic transport properties, *Carbon N. Y.* 50 (2012) 1338–1345. doi:http://doi.org/10.1016/j.carbon.2011.11.005.
- [15] X. Yi, W. He, X. Zhang, Y. Yue, G. Yang, Z. Wang, M. Zhou, L. Wang, Graphene-like carbon sheet/Fe<sub>3</sub>O<sub>4</sub> nanocomposites derived from soda papermaking black liquor for high performance lithium ion batteries, *Electrochim. Acta.* 232 (2017) 550–560. doi:http://dx.doi.org/10.1016/j.electacta.2017.02.130.
- [16] Z. Yang, D. Su, J. Yang, J. Wang, Fe<sub>3</sub>O<sub>4</sub>/C composite with hollow spheres in porous 3D-nanostructure as anode material for the lithium-ion batteries, *J. Power Sources.* 363 (2017) 161–167. doi:http://dx.doi.org/10.1016/j.jpowsour.2017.07.080.
- [17] H. Geng, S. Li, Y. Pan, Y. Yang, J. Zheng, H. Gu, Porous Fe<sub>3</sub>O<sub>4</sub> hollow spheres with chlorine-doped-carbon coating as superior anode materials for lithium ion batteries, *RSC Adv.* 5 (2015) 52993–52997. doi:10.1039/C5RA09915C.
- [18] F.-X. Ma, H. Hu, H. Bin Wu, C.-Y. Xu, Z. Xu, L. Zhen, X.W. (David) Lou, Formation of Uniform Fe<sub>3</sub>O<sub>4</sub> Hollow Spheres Organized by Ultrathin Nanosheets and Their Excellent Lithium Storage Properties, *Adv. Mater.* 27 (2015) 4097–4101. doi:10.1002/adma.201501130.
- [19] H. Li, R. Xu, Y. Wang, B. Qian, H. Wang, L. Chen, H. Jiang, Y. Yang, Y. Xu, In situ synthesis of hierarchical mesoporous Fe<sub>3</sub>O<sub>4</sub>@C nanowires derived from coordination polymers for high-performance lithium-ion batteries, *RSC Adv.* 4 (2014) 51960–51965. doi:10.1039/C4RA09110H.
- [20] K. Cheng, F. Yang, K. Ye, Y. Zhang, X. Jiang, J. Yin, G. Wang, D. Cao, Highly porous Fe<sub>3</sub>O<sub>4</sub>–Fe nanowires grown on C/TiC nanofiber arrays as the high performance anode of lithium-ion batteries, *J. Power Sources.* 258 (2014) 260–265. doi:https://doi.org/10.1016/j.jpowsour.2014.02.038.
- [21] Y. Jiao, H. Zhang, T. Dong, P. Shen, Y. Cai, H. Zhang, S. Zhang, Improved electrochemical performance in nanoengineered pomegranate-shaped Fe<sub>3</sub>O<sub>4</sub>/RGO nanohybrids anode material, *J. Mater. Sci.* 52 (2017) 3233–3243. doi:10.1007/s10853-016-0612-2.
- [22] Q.Q. Xiong, J.P. Tu, S.J. Shi, X.Y. Liu, X.L. Wang, C.D. Gu, Ascorbic acid-assisted synthesis of cobalt ferrite (CoFe<sub>2</sub>O<sub>4</sub>) hierarchical flower-like microspheres with enhanced lithium storage properties, *J. Power Sources.* 256 (2014) 153–159. doi:https://doi.org/10.1016/j.jpowsour.2014.01.038.
- [23] Q.Q. Xiong, J.P. Tu, Y. Lu, J. Chen, Y.X. Yu, Y.Q. Qiao, X.L. Wang, C.D. Gu, Synthesis of Hierarchical Hollow-Structured Single-Crystalline Magnetite (Fe<sub>3</sub>O<sub>4</sub>) Microspheres: The Highly Powerful Storage versus Lithium as an Anode for Lithium Ion Batteries, *J. Phys. Chem. C*. 116 (2012) 6495–6502. doi:10.1021/jp3002178.
- [24] C. Ding, Y. Zeng, R. Li, Y. Zhang, L. Zhao, Temperature- and time-tuned morphological evolution of polyhedral magnetite nanocrystals and their facet-dependent high-rate performance for lithium-ion batteries, *J. Alloys Compd.* 676 (2016) 347–355. doi:https://doi.org/10.1016/j.jallcom.2016.03.143.
- [25] D. Su, J. Horvat, P. Munroe, H. Ahn, A.R. Ranjbari, G. Wang, Polyhedral Magnetite Nanocrystals with Multiple Facets: Facile Synthesis, Structural Modelling, Magnetic Properties and Application for High Capacity Lithium Storage, *Chem. – A Eur. J.* 18 (2012) 488–497. doi:10.1002/chem.201101939.
- [26] Q. Lin, J. Wang, Y. Zhong, J. Sunarso, M.O. Tadé, L. Li, Z. Shao, High performance porous iron oxide-carbon nanotube nanocomposite as an anode material for lithium-ion batteries, *Electrochim. Acta.* 212 (2016) 179–186. doi:https://doi.org/10.1016/j.electacta.2016.06.135.
- [27] H. Tan, K. Huang, Y. Bao, Y. Li, J. Zhong, Rationally designed layer-by-layer structure of Fe<sub>3</sub>O<sub>4</sub> nanospheres@MWCNTs/graphene as electrode for lithium ion batteries with enhanced electrochemical

- performance, *J. Alloys Compd.* 699 (2017) 812–817. doi:<https://doi.org/10.1016/j.jallcom.2016.12.393>.
- [28] D. Xu, G. Luo, J. Yu, W. Chen, C. Zhang, D. Ouyang, Y. Fang, X. Yu, Quadrangular-CNT-Fe<sub>3</sub>O<sub>4</sub>-C composite based on quadrilateral carbon nanotubes as anode materials for high performance lithium-ion batteries, *J. Alloys Compd.* 702 (2017) 499–508. doi:<https://doi.org/10.1016/j.jallcom.2017.01.259>.
- [29] D. Yoon, J. Hwang, W. Chang, J. Kim, Uniform one-pot anchoring of Fe<sub>3</sub>O<sub>4</sub> to defective reduced graphene oxide for enhanced lithium storage, *Chem. Eng. J.* 317 (2017) 890–900. doi:<https://doi.org/10.1016/j.cej.2017.02.108>.
- [30] J. Jiao, W. Qiu, J. Tang, L. Chen, L. Jing, Synthesis of well-defined Fe<sub>3</sub>O<sub>4</sub> nanorods/N-doped graphene for lithium-ion batteries, *Nano Res.* 9 (2016) 1256–1266. doi:[10.1007/s12274-016-1021-1](https://doi.org/10.1007/s12274-016-1021-1).
- [31] Y. Suo, Q.-Q. Zhao, J.-K. Meng, J. Li, X.-C. Zheng, X.-X. Guan, Y.-S. Liu, J.-M. Zhang, Fabrication and electrochemical properties of 3D Fe<sub>3</sub>O<sub>4</sub>@graphene aerogel composites as lithium-ion battery anodes, *Mater. Lett.* 174 (2016) 36–39. doi:<https://doi.org/10.1016/j.matlet.2016.03.080>.
- [32] Y. Zhong, X. Zhou, X. Li, S. Zhang, Y. Liu, X. Yu, H. Wang, Q. Li, Y. Fang, J. Li, Sandwich-like mesoporous graphene@magnetite@carbon nanosheets for high-rate lithium ion batteries, *Solid State Sci.* 57 (2016) 16–23. doi:<https://doi.org/10.1016/j.solidstatesciences.2016.04.011>.
- [33] N. Zhang, C. Chen, X. Yan, Y. Huang, J. Li, J. Ma, D.H.L. Ng, Bacteria-inspired Fabrication of Fe<sub>3</sub>O<sub>4</sub>-Carbon/Graphene Foam for Lithium-Ion Battery Anodes, *Electrochim. Acta.* 223 (2017) 39–46. doi:<https://doi.org/10.1016/j.electacta.2016.12.006>.
- [34] N. Bi, X. Liu, N. Wu, C. Cui, Y. Sun, Improved electrochemical performance of onion-like carbon coated magnetite nanocapsules as electromagnetic absorptive anode materials for lithium-ion batteries, *RSC Adv.* 5 (2015) 32452–32459. doi:[10.1039/C5RA01627D](https://doi.org/10.1039/C5RA01627D).
- [35] M. Chen, X. Shen, K. Chen, Q. Wu, P. Zhang, X. Zhang, G. Diao, Nitrogen-doped Mesoporous Carbon-encapsulation Urchin-like Fe<sub>3</sub>O<sub>4</sub> as Anode Materials for High Performance Li-ions Batteries, *Electrochim. Acta.* 195 (2016) 94–105. doi:<https://doi.org/10.1016/j.electacta.2016.02.128>.
- [36] Q. Wu, R. Zhao, W. Liu, X. Zhang, X. Shen, W. Li, G. Diao, M. Chen, In-depth nanocrystallization enhanced Li-ions batteries performance with nitrogen-doped carbon coated Fe<sub>3</sub>O<sub>4</sub> yolk-shell nanocapsules, *J. Power Sources.* 344 (2017) 74–84. doi:<https://doi.org/10.1016/j.jpowsour.2017.01.101>.
- [37] M.N. Obrovac, V.L. Chevrier, Alloy Negative Electrodes for Li-Ion Batteries, *Chem. Rev.* 114 (2014) 11444–11502. doi:[10.1021/cr500207g](https://doi.org/10.1021/cr500207g).
- [38] R. Raccichini, A. Varzi, V.S.K. Chakravadhanula, C. Kübel, S. Passerini, Boosting the power performance of multilayer graphene as lithium-ion battery anode via unconventional doping with in-situ formed Fe nanoparticles, *Sci. Rep.* 6 (2016) 23585. <http://dx.doi.org/10.1038/srep23585>.
- [39] H. Sun, A. Varzi, V. Pellegrini, D.A. Dinh, R. Raccichini, A.E. Del Rio-Castillo, M. Prato, M. Colombo, R. Cingolani, B. Scrosati, S. Passerini, F. Bonaccorso, How much does size really matter? Exploring the limits of graphene as Li ion battery anode material, *Solid State Commun.* 251 (2017) 88–93. doi:<https://doi.org/10.1016/j.ssc.2016.12.016>.
- [40] L. Mohammed, H.G. Gomaa, D. Ragab, J. Zhu, Magnetic nanoparticles for environmental and biomedical applications: A review, *Particuology.* 30 (2017) 1–14. doi:<https://doi.org/10.1016/j.partic.2016.06.001>.
- [41] G. Mirabello, J.J.M. Lenders, N.A.J.M. Sommerdijk, Bioinspired synthesis of magnetite nanoparticles, *Chem. Soc. Rev.* 45 (2016) 5085–5106. doi:[10.1039/C6CS00432F](https://doi.org/10.1039/C6CS00432F).
- [42] L. Venosta, M. V Bracamonte, M.C. Rodríguez, S.E. Jacobo, P.G. Bercoff, Comparative studies of hybrid functional materials based on different carbon structures decorated with nano-magnetite. Suitable application as platforms for enzyme-free electrochemical sensing of hydrogen peroxide, *Sensors Actuators B Chem.* 248 (2017) 460–469. doi:[http://doi.org/10.1016/j.snb.2017.03.159](https://doi.org/10.1016/j.snb.2017.03.159).
- [43] S. Zhu, J. Guo, J. Dong, Z. Cui, T. Lu, C. Zhu, D. Zhang, J. Ma, Sonochemical fabrication of Fe<sub>3</sub>O<sub>4</sub> nanoparticles on reduced graphene oxide for biosensors, *Ultrason. Sonochem.* 20 (2013) 872–880. doi:[http://dx.doi.org/10.1016/j.ultsonch.2012.12.001](https://doi.org/10.1016/j.ultsonch.2012.12.001).
- [44] M.V. Bracamonte, M. Melchionna, A. Giuliani, L. Nasi, C. Tavagnacco, M. Prato, P. Fornasiero, H<sub>2</sub>O<sub>2</sub> sensing enhancement by mutual integration of single walled carbon nanohorns with metal oxide catalysts: The CeO<sub>2</sub> case, *Sensors Actuators B Chem.* 239 (2017) 923–932. doi:[http://dx.doi.org/10.1016/j.snb.2016.08.112](https://doi.org/10.1016/j.snb.2016.08.112).
- [45] M. Gauthier, T.J. Carney, A. Grimaud, L. Giordano, N. Pour, H. Chang, D.P. Fenning, S.F. Lux, O. Paschos, C.

- Bauer, F. Maglia, S. Lupart, P. Lamp, Y. Shao-horn, Electrode-Electrolyte Interface in Li-Ion Batteries: Current Understanding and New Insights, *J. Phys. Chem. Lett.* 6 (2015) 4653–4672. doi:10.1021/acs.jpcllett.5b01727.
- [46] M.D. Levi, D. Aurbach, The mechanism of lithium intercalation in graphite film electrodes in aprotic media. Part 1. High resolution slow scan rate cyclic voltammetric studies and modeling, *J. Electroanal. Chem.* 421 (1997) 79–88. doi:http://dx.doi.org/10.1016/S0022-0728(96)04832-2.
- [47] B. Markovsky, M.D. Levi, D. Aurbach, The basic electroanalytical behavior of practical graphite–lithium intercalation electrodes, *Electrochim. Acta.* 43 (1998) 2287–2304. doi:https://doi.org/10.1016/S0013-4686(97)10172-4.
- [48] Y.-Y. Hu, Z. Liu, K.-W. Nam, O.J. Borkiewicz, J. Cheng, X. Hua, M.T. Dunstan, X. Yu, K.M. Wiaderek, L.-S. Du, K.W. Chapman, P.J. Chupas, X.-Q. Yang, C.P. Grey, Origin of additional capacities in metal oxide lithium-ion battery electrodes, *Nat Mater.* 12 (2013) 1130–1136. http://dx.doi.org/10.1038/nmat3784.
- [49] S. Krehula, S. Musić, Influence of ruthenium ions on the precipitation of  $\alpha$ -FeOOH,  $\alpha$ -Fe<sub>2</sub>O<sub>3</sub> and Fe<sub>3</sub>O<sub>4</sub> in highly alkaline media, *J. Alloys Compd.* 416 (2006) 284–290. doi:http://dx.doi.org/10.1016/j.jallcom.2005.09.016.
- [50] M.D. Levi, D. Aurbach, Impedance spectra of porous, composite intercalation electrodes: The origin of the low-frequency semicircles, *J. Power Sources.* 146 (2005) 727–731. doi:https://doi.org/10.1016/j.jpowsour.2005.03.164.

**FIGURES & TABLES CAPTIONS**

**Figure 1.** TEM images of Fe<sub>3</sub>O<sub>4</sub>-G2 (**A**), Fe<sub>3</sub>O<sub>4</sub>-G17 (**B**) and Fe<sub>3</sub>O<sub>4</sub>-G410 (**C**). SEM images of the anodes of Fe<sub>3</sub>O<sub>4</sub>-G2 (**D**), Fe<sub>3</sub>O<sub>4</sub>-G17 (**E**) and Fe<sub>3</sub>O<sub>4</sub>-G410 (**F**).

**Figure 2.** XRD patterns for the slurries made of Fe<sub>3</sub>O<sub>4</sub>-G2 (**a**), Fe<sub>3</sub>O<sub>4</sub>-G17 (**b**) and Fe<sub>3</sub>O<sub>4</sub>-G410 (**c**). Reflection peaks indexed with (\*) correspond to the spinel phase of magnetite and the peaks corresponding to the reflections of hexagonal structure of graphite are indexed with (●).

**Figure 3.** TGA profiles for G2 (**A**), G17 (**B**) and G410 (**C**) samples, performed in air at a heating rate of 10 °C min<sup>-1</sup>. The dashed lines correspond to the thermograms of pure graphite samples and the full lines, to the Fe<sub>3</sub>O<sub>4</sub>-G hybrids.

**Figure 4.** Representative CV curves (scan rate = 0.0001 Vs<sup>-1</sup>) of the 1st (grey lines) and 5th cycle for the Fe<sub>3</sub>O<sub>4</sub>-G2 (**A**), Fe<sub>3</sub>O<sub>4</sub>-G17 (**B**) and Fe<sub>3</sub>O<sub>4</sub>-G410 (**C**) hybrid anodes. The contribution to the current of the lithiation/delithiation of Fe<sub>3</sub>O<sub>4</sub> (red lines) and graphite (blue lines) are depicted at the 5th cycle.

**Figure 5.** Representative galvanostatic lithiation profile (black curve and axes) and the derived dQ/dV plot (blue curve and axes) at 0.10 Ag<sup>-1</sup> for the Fe<sub>3</sub>O<sub>4</sub>-G2 (**A**), Fe<sub>3</sub>O<sub>4</sub>-G17 (**B**) and Fe<sub>3</sub>O<sub>4</sub>-G410 (**C**) anodes. The red-shaded region corresponds to the Fe<sub>3</sub>O<sub>4</sub> conversion reaction and the grey-shaded one, to the graphite intercalation reaction.

**Figure 6.** Rate capabilities (full symbols) and coulombic efficiencies (empty symbols) of Fe<sub>3</sub>O<sub>4</sub>-G2 (●), Fe<sub>3</sub>O<sub>4</sub>-G17 (■) and Fe<sub>3</sub>O<sub>4</sub>-G410 (▲) hybrid anodes at various current densities. The specific capacities correspond to the lithiation cycle.

**Figure 7.** EIS spectra of Fe<sub>3</sub>O<sub>4</sub>-G2 (■), Fe<sub>3</sub>O<sub>4</sub>-G17 (●) and Fe<sub>3</sub>O<sub>4</sub>-G410 (▲) hybrid anodes taken at 3.000 V (delithiated, **A**) and at 0.010 V (lithiated, **B**). The full lines represent the fittings with the appropriate equivalent circuit. Conditions: E<sub>dc</sub> = o.c.p., amplitude = 5 mV, frequency range = 10<sup>5</sup> – 10<sup>2</sup> Hz.

**Figure 8.** Variation of R<sub>ct</sub> (**A**) and R<sub>SEI</sub> (**B**) with the graphite flake size of Fe<sub>3</sub>O<sub>4</sub>-G hybrids anodes obtained from EIS spectra of **Figure 7**, at delithiated 3.000 V (black bars) and lithiated 0.010 V (red bars) states. (**C**) Variation of R<sub>pore</sub> (left axis) and Q<sub>pore</sub> (right axis) with the G flake size of Fe<sub>3</sub>O<sub>4</sub>-G hybrids anodes obtained from EIS spectra of **Figure 7 B**, at lithiated 0.010 V.

**Scheme 1.** Equivalent circuit for delithiated anodes.

**Scheme 2.** Equivalent circuit for lithiated anodes.

**FIGURE 1**

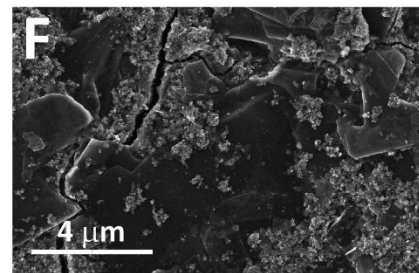
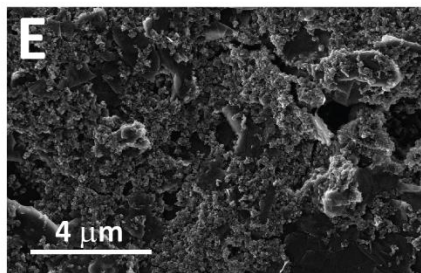
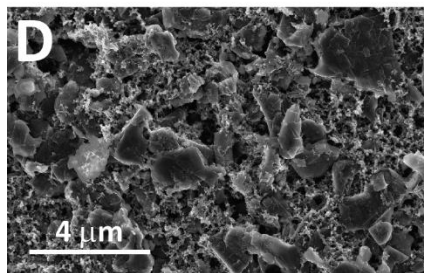
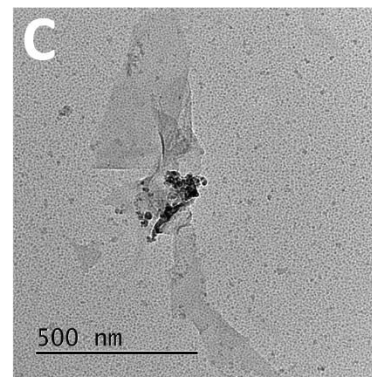
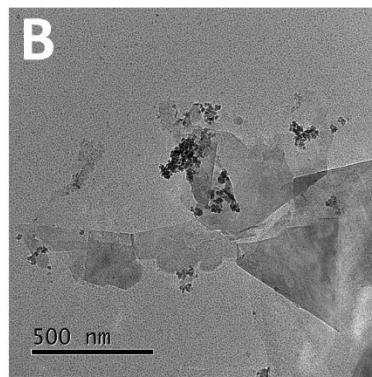
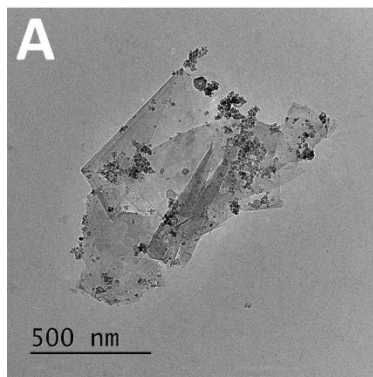


FIGURE 2

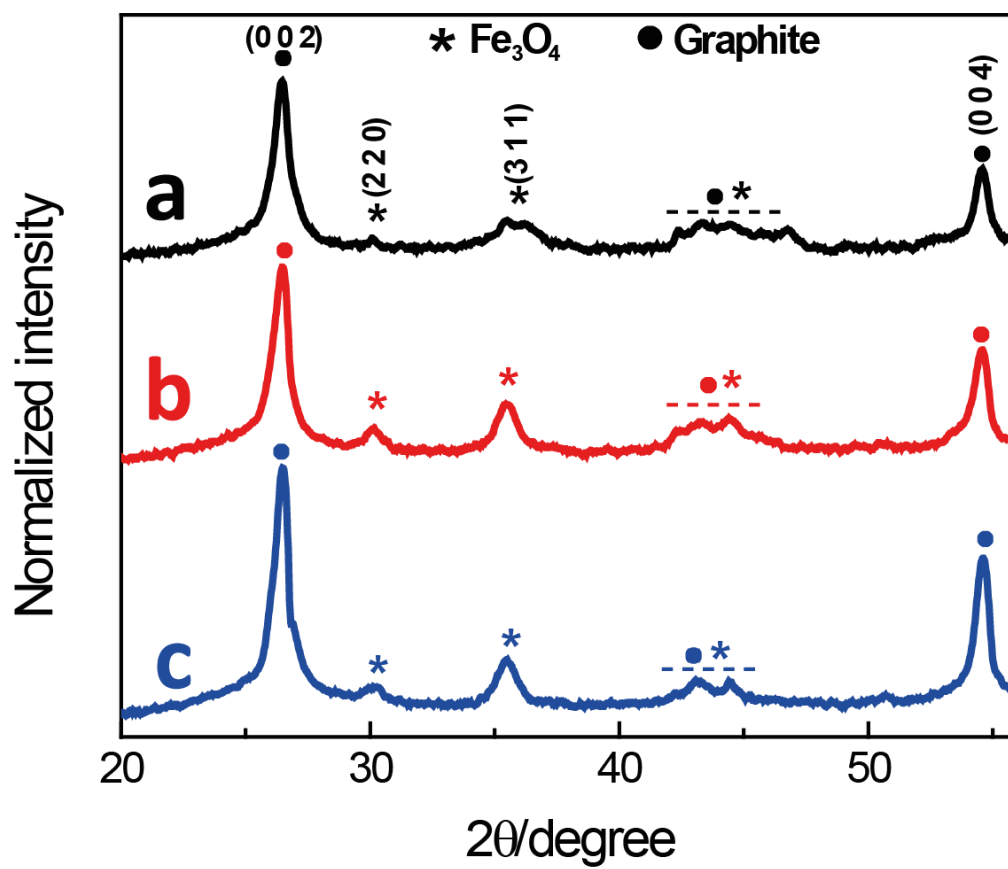


FIGURE 3

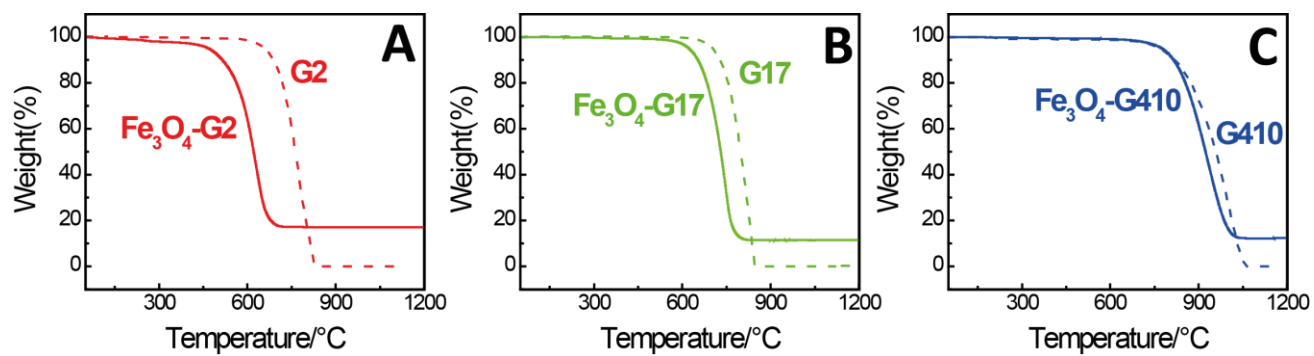


FIGURE 4

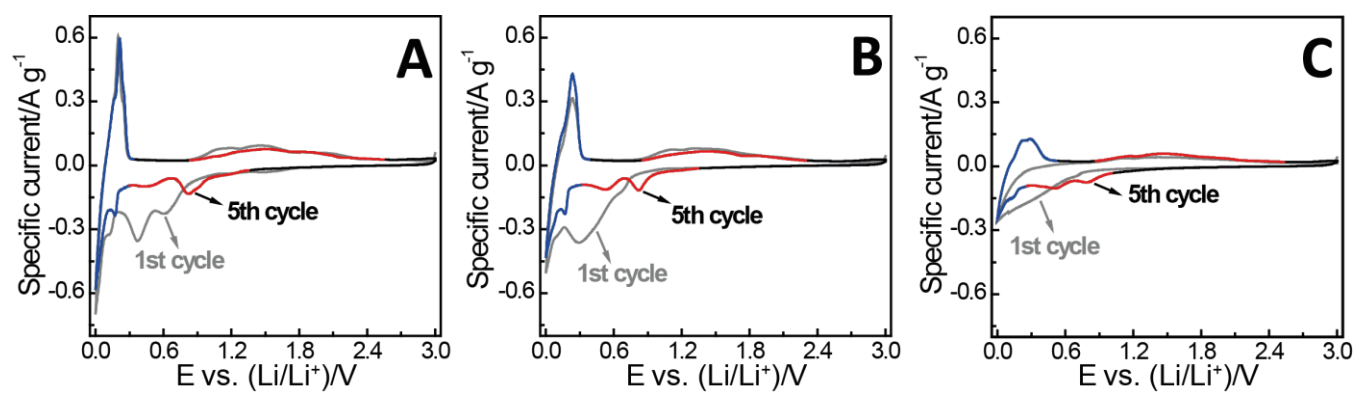


FIGURE 5

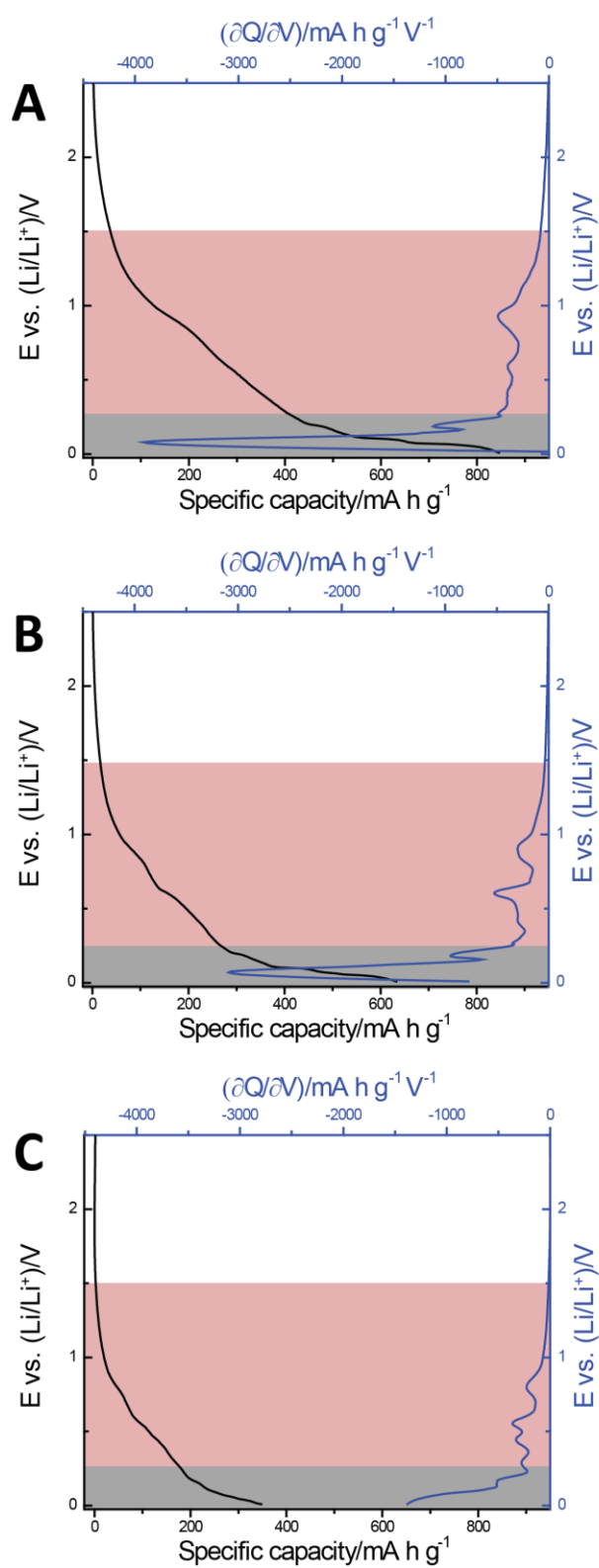


FIGURE 6

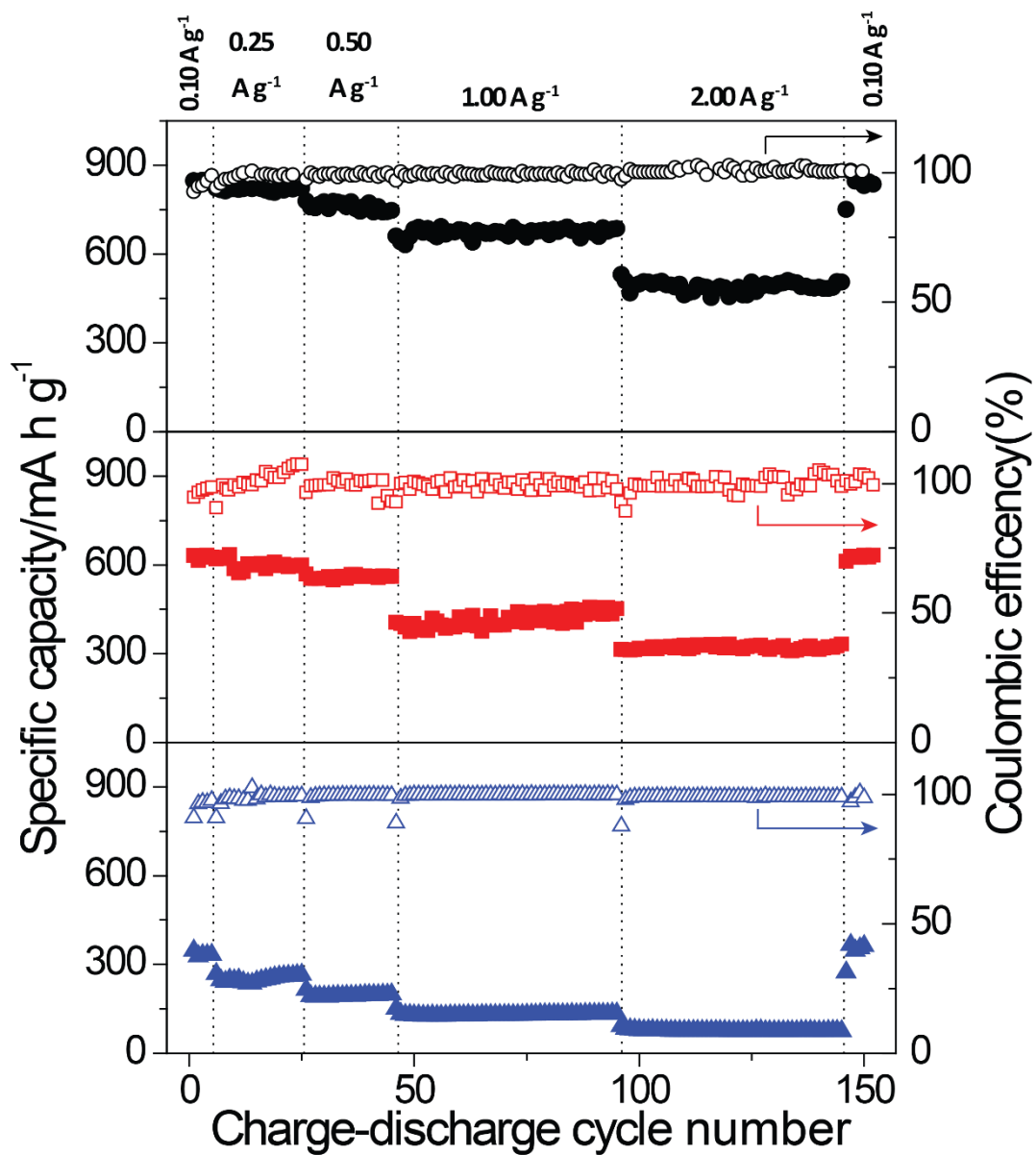


FIGURE 7

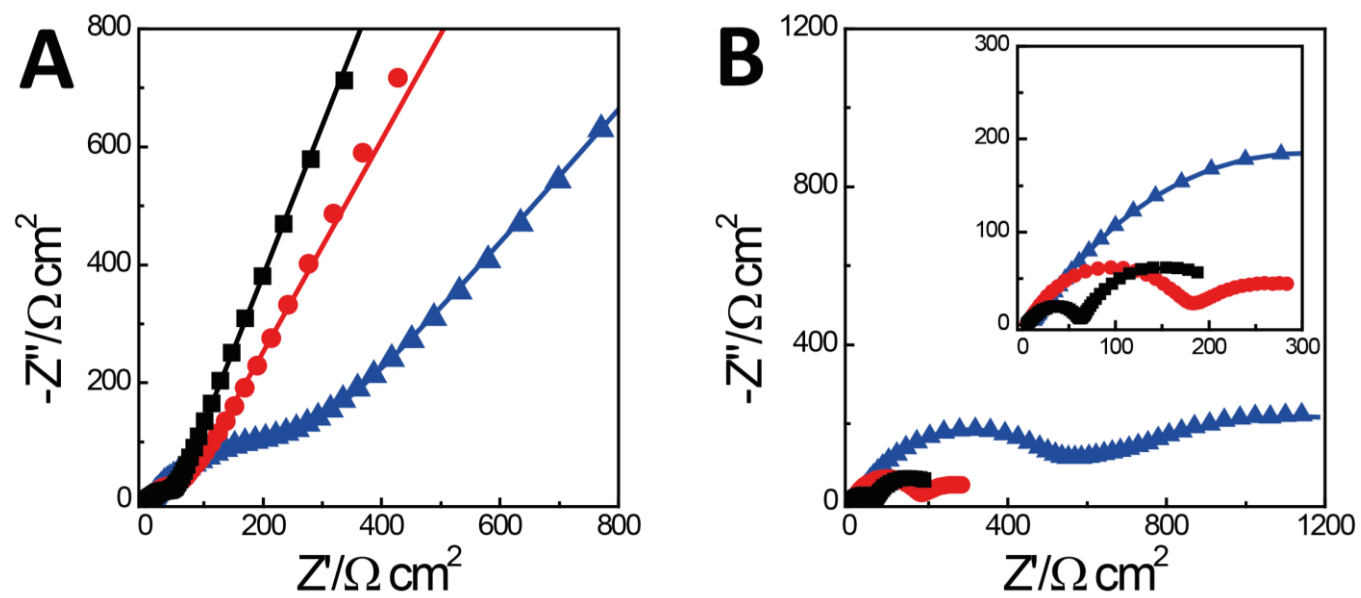
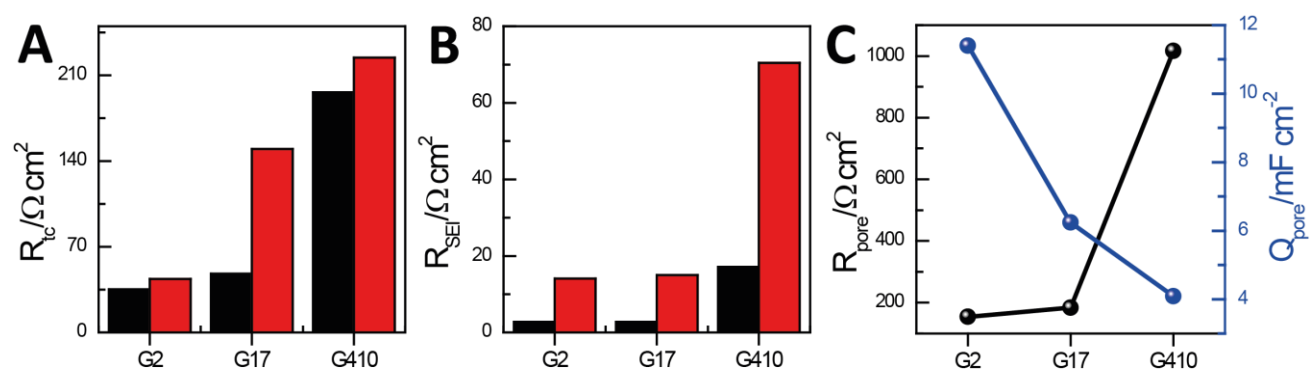
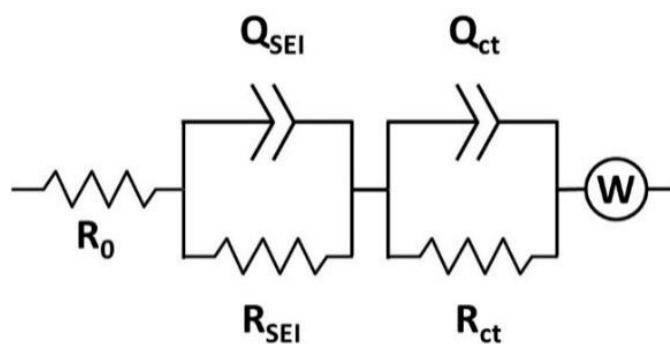


FIGURE 8



## SCHEME 1



## SCHEME 2

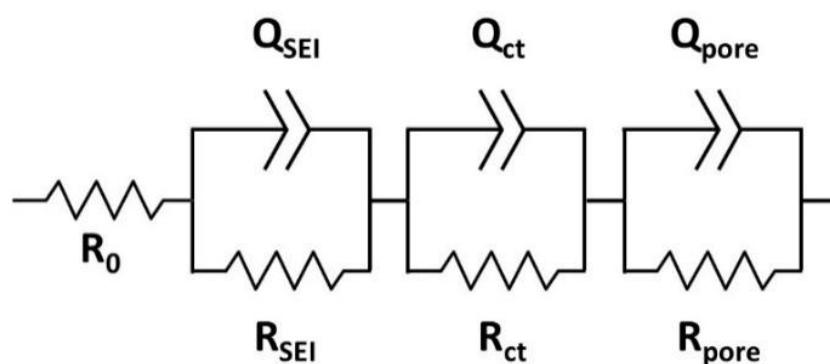


**Table 1.** Onset temperatures ( $T_0$ ) for graphites and  $\text{Fe}_3\text{O}_4$ -G hybrids, and  $\text{Fe}_3\text{O}_4$ -loadings of each sample. The data were calculated from the TGA profiles of **Figure 3**.

## TABLE 1

Onset temperatures/ $^{\circ}\text{C}$		$\text{Fe}_3\text{O}_4$ content(wt%)
without $\text{Fe}_3\text{O}_4$	with $\text{Fe}_3\text{O}_4$	

Fe <sub>3</sub> O <sub>4</sub> -G2	700	550	16
Fe <sub>3</sub> O <sub>4</sub> -G17	745	666	11
Fe <sub>3</sub> O <sub>4</sub> -G410	874	828	12

**Table 2.** Specific capacities and coulombic efficiencies for the Fe<sub>3</sub>O<sub>4</sub>-G hybrids anodes and Fe<sub>3</sub>O<sub>4</sub> lithiation contribution to the total specific capacity of each hybrid. The data were obtained from the charge-discharge profiles presented in **Figure 5**.

	Specific capacity/mA h g <sup>-1</sup>	Coulombic efficiency(%)	Fe <sub>3</sub> O <sub>4</sub> contribution to specific capacity(%) *
Fe <sub>3</sub> O <sub>4</sub> -G2	845	98.9	42
Fe <sub>3</sub> O <sub>4</sub> -G17	633	98.1	34
Fe <sub>3</sub> O <sub>4</sub> -G410	348	96.0	43

\* Calculated as the ratio between the specific capacity in the Fe<sub>3</sub>O<sub>4</sub> lithiation region (between 1.500 and 0.250 V) and the total specific capacity.